Solid-State Electronics 77 (2012) 64–71

Contents lists available at SciVerse ScienceDirect

Solid-State Electronics

journal homepage: www.elsevier.com/locate/sse

Design and fabrication of MEMS-based thermally-actuated image stabilizer for cell phone camera

Chun-Ying Lin [a], Jin-Chern Chiou [a,b,*]

[a] Department of Electrical and Control Engineering, National Chiao Tung University, Hsin-Chu, Taiwan, ROC
[b] School of Medicine, China Medical University, Taichung, Taiwan, ROC

ARTICLE INFO

Article history:
Available online 29 June 2012

Keywords:
Component
XY stage
Image stabilizer
MEMS
Thermal actuator

ABSTRACT

A micro–electro-mechanical system (MEMS)-based image stabilizer is proposed to counteracting shaking in cell phone cameras. The proposed stabilizer (dimensions, $8.8 \times 8.8 \times 0.2$ mm^3) includes a two-axis decoupling *XY* stage and has sufficient strength to suspend an image sensor (IS) used for anti-shaking function. The *XY* stage is designed to send electrical signals from the suspended IS by using eight signal springs and 24 signal outputs. The maximum actuating distance of the stage is larger than 25 μm, which is sufficient to resolve the shaking problem. Accordingly, the applied voltage for the 25 μm moving distance is lower than 20 V; the dynamic resonant frequency of the actuating device is 4485 Hz, and the rising time is 21 ms.

© 2012 Elsevier Ltd. All rights reserved.

1. Introduction

Advances in device miniaturization and high precision systems now enable micro fabrication of *XY* stages [1]. One of the most common actuators used to drive MEMS-based *XY* stages is the electrostatic actuator, which is often used in optical applications [2–7] and probe position systems [8] because it has good controllability and low power consumption; applications of the electrostatic *XY* stage include SPM (Scanning Probe Microscopy) probe [9,10,12], data storage [11–15], and nano-position control [1,16–18]. However, since electrostatic actuators often require a high driving voltage, the step-up circuit must be very large. To decrease driving voltage and to increase actuating force, thermal actuators are used to increase actuating displacement [25].

The camera function has a growing role in cell phone applications. In addition to meeting the consumer demand for increased pixels, digital single lens reflex (DSLR) camera functions are now being embedded in commercial cell phones. Anti-shake technology is among the many new technologies developed for mobile phones. Since increasing the number of camera pixels exacerbates the problem of image blurring caused by hand shaking, an effective image stabilization method is needed [19]. The most common image stabilization methods include lens shifting [20], CCD shifting [21], and signal processing [22]. Signal processing, which is the anti-shaking technique conventionally used in DSLRs, is now used in mobile phones. Although signal processing requires no additional hardware and does not affect miniaturization of the system module, performance and reliability depend on the algorithm used, thus signal processing method usually require large memory. Given the demand for device miniaturization, the lens shifting anti-shaking approach is inadequate since adding a movable lens causes nonlinearity that requires compensation with a complex control algorithm. Although it requires an actuating system, IS shifting is less disruptive of miniaturization; the overall size of the system is also easier to reduce compared to lens shifting method [19]. The MEMS device enables precise movement of suspended microstructures and monolithic integration with microelectronic circuits on a chip [23]. Therefore, an effective image stabilizer design is needed to miniaturize cell phone camera modules.

The MEMS-based two dimensional decoupling thermal actuating *XY* stage proposed in this study has several advantages: 1. Small chip size: since the presented *XY* stage is fabricated by MEMS process, the dimensions are smaller than those of other commercial anti-shaking devices. 2. Low driving voltage: the thermal actuating mechanism requires a lower driving voltage and smaller step-up circuit compared to conventional actuators. 3. Simple control method: the CCD shifting approach directly compensates for blurred pixels, so complex control algorithms and optical path designs are not needed.

The image stabilizer design is suitable for a cell phone equipped with a 3× optical zoom, an actuator that can move at least 25 μm [19], and a sufficiently strong structure to withstand a $3.5 \times 3.5 \times 0.1$ mm^3 IS load, from which it must be decoupled in two dimensions when driven. Therefore, the proposed design has a high aspect ratio and 50 μm-thick silicon springs. Four decoupling springs for the main suspended and decoupling structures

* Corresponding author at: School of Medicine, China Medical University, Taichung, Taiwan, ROC
E-mail address: chiou@mail.nctu.edu.tw (J.-C. Chiou).

0038-1101/$ - see front matter © 2012 Elsevier Ltd. All rights reserved.
http://dx.doi.org/10.1016/j.sse.2012.05.013

connect with the shuttle. The fabrication process used to manufacture the device includes double-side lithography, two ICP etching processes, and flip–chip bonding process. The output routing for electrical connection of the IS includes 24 signal outputs from eight signal springs. The required 25 μm displacement is achieved when driven in a moving direction lower than 20 DC voltages, and the decoupling effect in the opposite direction is excellent.

2. Concept and structure design

The novel feature of the proposed MEMS-based image stabilizer is a 2D decoupling actuator that can carry an IS to compensate for blurring caused by shaking. The design of the *XY* stage is described below.

2.1. Design of XY stage

The proposed image stabilizer is designed to provide excellent decoupling performance and to minimize the size of the device used for suspending the IS. The anti-shaking function is provided by a decoupling structure that compensates for shaking with no additional moving deviation in another direction. Fig. 1a shows a simple schematic diagram of the proposed decoupling main structure. When a single direction force $\boldsymbol{F_x}$ is applied to the decoupling structure, displacement $\boldsymbol{\Delta x}$ occurs only in the direction parallel to the driving force, and displacement in the opposite direction is negligible. Fig. 1b illustrates a simplified operating mechanism of the proposed decoupling *XY* stage when different forces are applied in the *x*- and *y*-directions. The decoupling design assumes perfect displacement in the *x*- and *y*-directions ($\boldsymbol{\Delta x}$ and $\boldsymbol{\Delta y}$, respectively) and assumes perfect mechanical isolation between the two orthogonal driving directions.

The proposed for suspending the IS has a thickness of 50 μm to provide sufficient stiffness in the *z*-direction. Circuit routing of signal outputs must be patterned on the device layer. The signal springs and pads must be designed to maintain a working electrical connection. Flip–chip bonding, wire bonding, routing springs, and electrode pads are used to obtain an electrical connection between cell phone circuits in the IS pads and the electrode pads in the device structure and also between the electrode pads in the device structure and the output of the PCB pads. Fig. 2 schematically depicts the entire device. Separate decoupling beams are used in each direction to satisfy the kinematic design requirements shown in Fig. 1. Each thermal-driven actuator has a push-only design, and each operates in only one direction, i.e., *X*+, *X*−, *Y*+, or *Y*−. In the symmetrical spring design, the electrical routings are arranged in a balanced layout with two signal output springs and pads in each direction. The signal output springs are designed to be as thin as possible so that stiffness does not affect the overall spring constant system. The isolation layers and the isolator SU-8 ensure that the electric potential between each structure and signal output is independent.

2.2. Operating principles of electro-thermal chevron actuator

The proposed image stabilizer is driven by electro-thermal mechanical force. Fig. 3 shows a simple schematic diagram of the electro-thermal chevron actuator of the proposed image stabilizer. An electro-thermal mechanical force generated by applying a voltage to the pads changes the relative displacement between the *XY* stage and pads.

When estimating driving displacement, several boundary conditions are assumed: 1. The actuator is heated uniformly, 2. Pad temperatures are fixed at 300 K, and 3. The expansion coefficient is a constant equal to Si expansion coefficient, 2.5 ppm/K. Under these conditions, the driving displacement is linearly related to temperature. The equation for predicting driving displacement is given below [26]:

$$EI\frac{\partial^2 y}{\partial x^2} = M = M_A - Fy - F_o x/2 \tag{1}$$

where boundary conditions are

$$y|_{x=0} = 0; \left.\frac{\delta y}{\delta x}\right|_{x=0} = \left.\frac{\delta y}{\delta x}\right|_{x=L/2} = \tan\theta_A; \sigma = \Delta TE\alpha = \frac{E}{L}\left(\Delta L + \frac{FL}{EWT}\right) \tag{2}$$

where *EI* is the flexural rigidity, *F* is the reaction force along *x*-axis used to model the effects of thermal stress, and F_o is the output force. The *L*, *W* and *T* in Fig. 3 are the length, width and thickness of the actuator, respectively. The ΔT is the temperature change, ΔL is the change in *L* due to *F*, and α is the thermal expansion

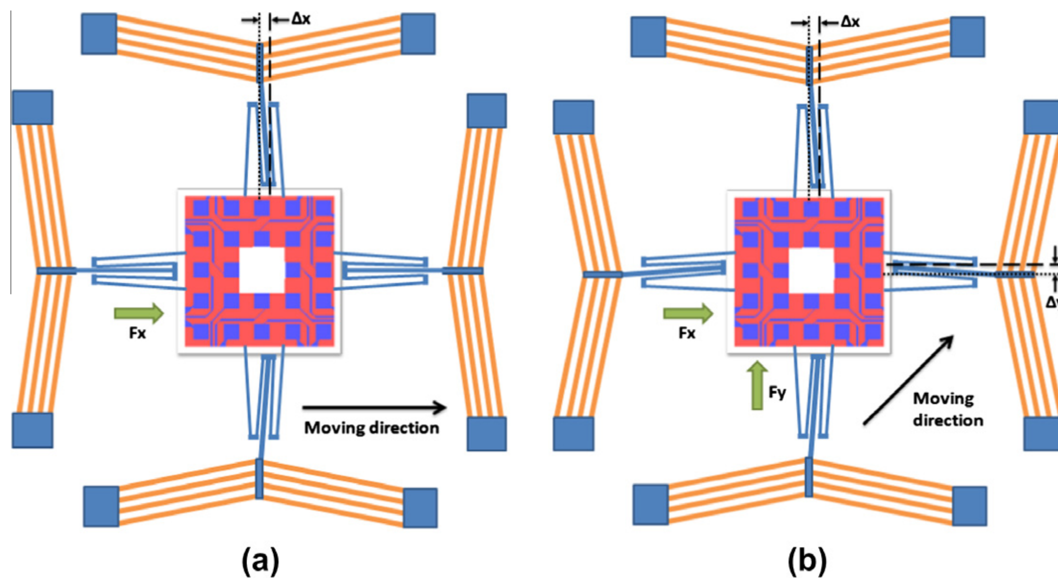

Fig. 1. Illustration of driving modes of decoupling *XY* stage: (a) in *X*-direction only and (b) in both *X*- and *Y*-directions.

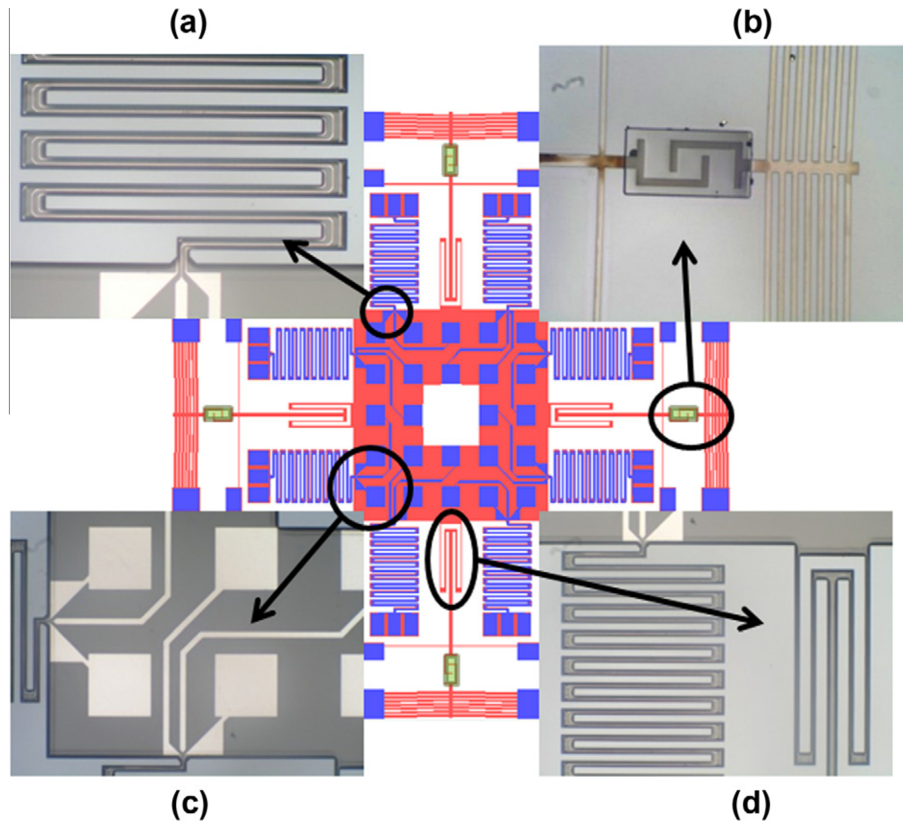

Fig. 2. Structure of *XY* stage, (a) Signal output beam (b) thermal actuator and SU8 isolator (c) electrode pads (d) decouple beam.

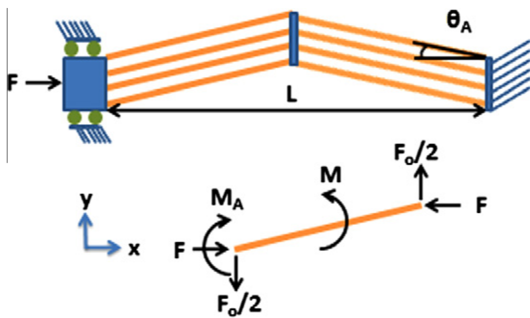

Fig. 3. Force acting on the chevron thermal actuator.

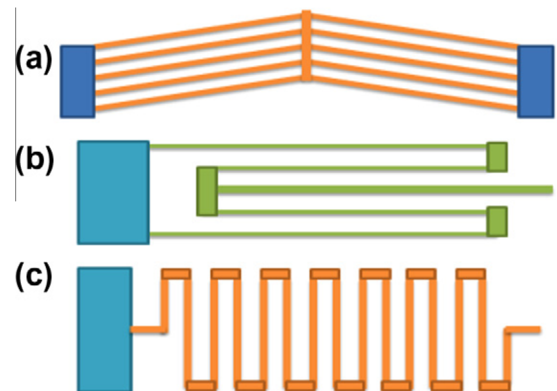

Fig. 4. Illustrations of (a) chevron thermal actuator beams, (b) decoupling beams and (c) folded flexure beams.

coefficient. Peak deflection is obtained by setting output force to zero, and peak output force is obtained by setting deflection to zero. The equation used to derive the relationship between the lateral force for peak deflection and peak output force is

$$F_{omax} = 2F_{max} \tan \theta_A \tag{3}$$

The equation also gives peak output force according to peak deflection. The output force and displacement can be calculated by modifying the actuator beam dimensions and gradients.

2.3. Designing and estimating spring stiffness

Fig. 4 shows the three flexure beams used in this work. Fig. 4a is a chevron thermal actuator. The small pre-bending angle can be simplified as parallel clamped–clamped beams [10,12]. According to Ref. [27], the decoupling ratio for the decoupling beam in Fig. 4b must be larger than 10 when the pixel size and the maximum actuating displacement are 2.5 μm and 25 μm, respectively.

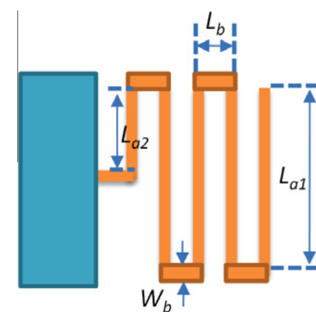

Fig. 5. Illustration of folded-flexure spring.

Table 1
Flexure beam specifications.

Spring type	Fig. 4a	Fig. 4b	Fig. 4c
Length	$La1$:630 μm $La2$:300 μm	L:2000 μm	$La1$:900 μm $La2$:790 μm
Width	30 μm	20 μm	25 μm
Height	50 μm	50 μm	50 μm

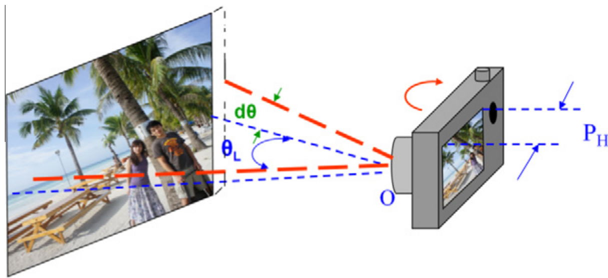

Fig. 6. Relationship between blurred pixels and hand shaking angle.

Fig. 4c is an IS signal output beam. Fig. 5 shows the spring design of the structure [11,13], and the flexure beam specifications of Fig. 4 in this work are shown in Table 1.

2.4. Motion range analysis of decoupling XY stage

Most commercially available cell phones have multi-megapixel cameras but lack an anti-shaking function. Because shaking is difficult to avoid when using a cell phone camera, blurring is common. Fig. 6 displays the relationship between the number of blurred pixels and the angle of hand shaking. When the camera moves through an angle $d\theta$ in the horizontal plane, the number of blurred pixels can be represented as

$$BP = \frac{d\theta}{\theta_L} P_H \quad (4)$$

where θ_L denotes the horizontal angle and P_H denotes the total number of horizontal pixels. Cell phone cameras typically have an angular field of view ranging from 35° to 45°. For an IS with a 45° field of view, experimental data [24] show that, within a 2 s period, hand shaking can cause horizontal drift of up to 0.08°. The device proposed in this work contains a three-megapixel (2056 × 1544 pixels) IS. According to Eq. (4), each pixel corresponds to a horizontal angle of 0.022°. Therefore, the number of blurred horizontal pixels is approximately 3.7. Since pixel size is 2.2 × 2.2 μm^2, the blurred image can only be adjusted if the range of motion in the XY stage is larger than 8.14 μm. Since many commercially available cameras have a 3× zoom function, the range of motion must be threefold higher than this value, i.e., 24.42 μm.

3. System modeling and FEA simulation

The decoupling effect, stiffness and the natural frequency of the designed image stabilizer is elucidated in a simulated actuator constructed using Intellisuite finite elements analysis (FEA) software. The software is used for static simulations of in-plane distance and the coupled mechanical interference of the image stabilizer in each orthogonal direction. In dynamic simulation, this software simulates the resonant frequency.

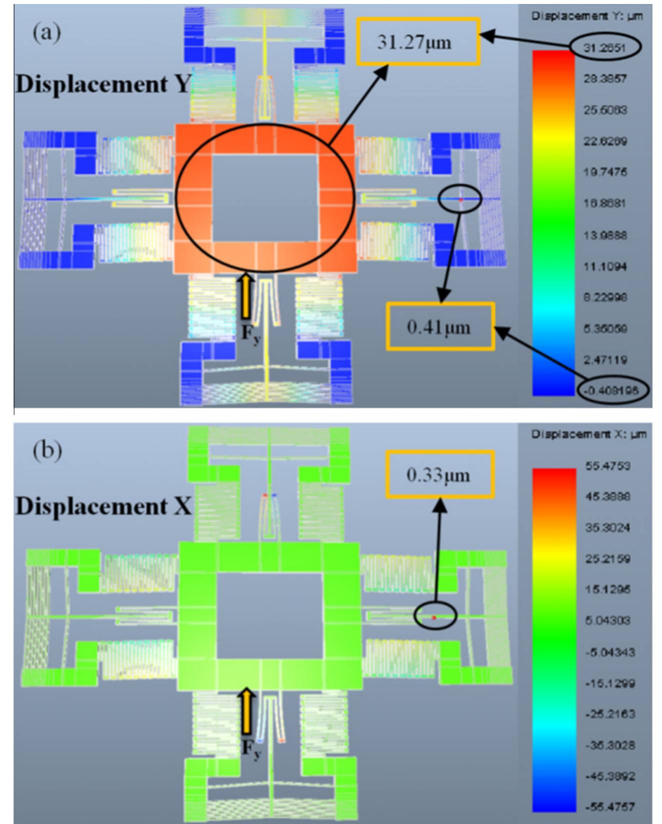

Fig. 7. Schematic of decoupling simulation in (a) the Y-direction and (b) the X-direction when the main structure of image stabilizer is driven with an outside force in the Y-direction.

3.1. Simulated decoupling of main structure

This section describes the design and simulation of the decoupling structure, and Fig. 7 shows the simulation results for the decoupling effect. Notably, non-decoupling relative structures are excluded. Four major decoupling springs are designed to connect with the chevron thermal actuator. The simulated decoupling effect of the main structure is based on the following actual boundary conditions: 1. The anchor is ignored since it is bonded with a substrate and does not affect the simulation results. 2. The shuttle, decoupling and flexure beams are suspended above the substrate. If the moldings of the designed moving spring and a frame-loaded spring are the same size as the image stabilizer, a significant decoupling effect occurs in the x and y directions (Fig. 7a and b, respectively). In the simulation, a specific force F_y in the y-direction causes a 31.27 μm displacement in the y-direction. Simulation results indicate that the displacement in the x-direction is only 0.33 μm. The simulated decoupling ratio in the x and y directions confirms the excellent decoupling effect in the design of the movable springs, which clearly meets the decoupling requirement.

3.2. Simulated structural stiffness and actuator force output

The stiffness and force output of thermal actuators in the XY stage are simulated in three steps. First, establish a reference beam where the width, length, thickness and folding number are 20 μm, 320 μm, 50 μm and 8 μm, respectively, and apply a force of 1000 μN to the reference beam Then use Hooke law to calculate displacement and stiffness. Fig. 8a shows the simulation results. Second, apply 1000 μN to the actuator, and observe the displacement to determine actuator stiffness for different series of numbers

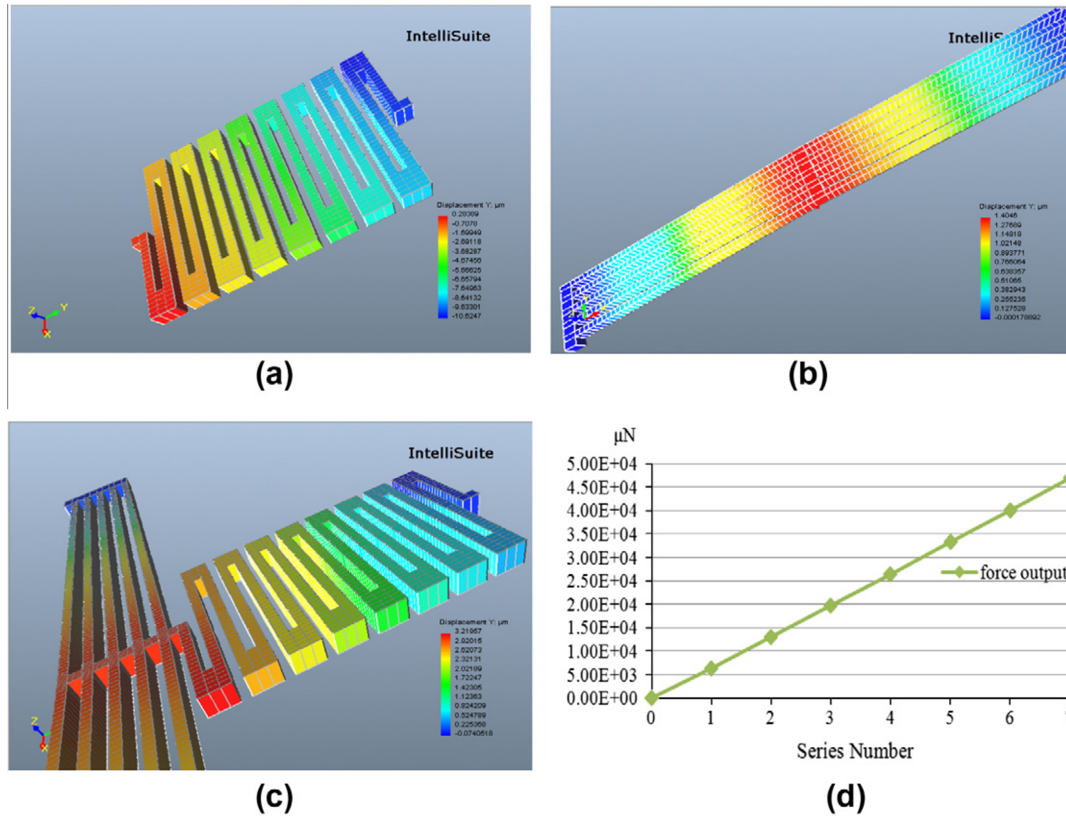

Fig. 8. (a) Reference beam displacement; (b) actuator beam displacement; (c) actuator displacement when apply 1000 μN. (d) Force output *versus* series number of thermal actuators.

(Fig. 8b). Third, connect the reference beam with thermal actuators of several series numbers, and apply a voltage to simulate the force output (Fig. 8c).

Table 2 shows the stiffness, displacement and force output of series numbers 1–7, where series number is thermal actuator number, *Disp.* is actuating displacement, K_a is actuator stiffness, and K_r is reference beam stiffness. Force outputs are calculated using Eq. (5), and Fig. 8d plots the results. The simulation results show a linear relationship between series number and force output. However, power consumption correlates positively with series

$$F = (K_a + K_r) * Disp. \tag{5}$$

3.3. Simulated dynamic frequency

To determine the resonant frequency and shapes of the designed structure, an instantaneous analysis is performed using Intellisuite FEM software is performed to verify the vibration characteristics. The simulated flexure structures are completely reserved and modeled, and the calculated weights of the shuttle and IS indicate that they are equivalent to those of the other structures. The following equation gives the resonant frequency.

$$F_{resonant} = \frac{1}{2\pi}\sqrt{\frac{k}{M}} \tag{6}$$

where k is the system stiffness of the image stabilizer, M is the overall weight of the image stabilizer, and $F_{resonant}$ is the resonant frequency of the *XY* stage. Because the structure is symmetrical, the simulated resonant frequency of the first mode is 4660 Hz with movement in *x*-direction and in *y*-direction.

Table 2
Simulation results.

Series number	*Disp.* (μm)	K_a	K_r	*F* (μN)
1	27.16	137.36	91.74	6222
2	34.62	283.29	91.74	12,984
3	38.03	425.53	91.74	19,672
4	40.00	568.18	91.74	26,397
5	41.3	714.28	91.74	33,289
6	42.25	854.7	91.74	39,987
7	42.96	1000	91.74	46,901

4. Fabrication

4.1. Fabrication processes

The fabrication steps are device layer formation, substrate formation, and the final combination of IS and *XY* stage. Fig. 9 depicts the device layer fabrication process. This segment performs the steps required for device layer formation, including structure definition, heat isolation, circuit routing and electric isolation. Fabrication begins with a (100) SOI wafer, where the thicknesses of the device layer, isolator and substrate are 50 μm, 2 μm and 350 μm, respectively. The fabrication process is performed in the following steps:

a. After basic RCA cleaning, use CVD process to deposit a 0.5 μm-thick nitride layer on the topside and a 2 μm-thick silicon oxide layer on the backside of the SOI wafer (Fig. 9a).
b. During photolithography, pattern the nitride as the electric isolation between the shuttle and circuit on the SOI wafer topside (Fig. 9b).

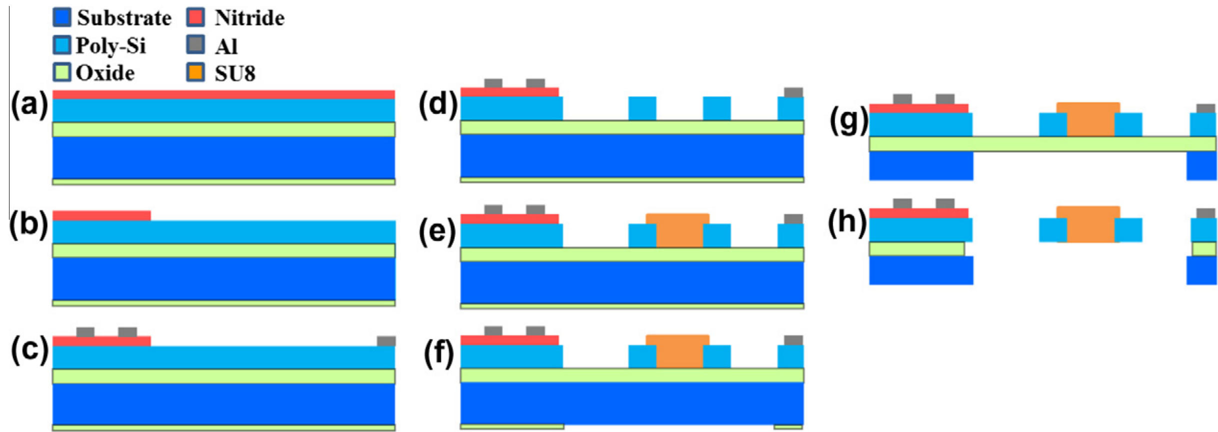

Fig. 9. Fabrication process for the *XY* stage: (a) backside oxide and nitride deposition (oxide: 2 μm, nitride: 0.5 μm), (b) nitride patterning, (c) Al patterning (1 μm), (d) device layer patterning, (e) SU8 patterning, (f) backside oxide patterning, (g) backside layer patterning (350 μm), and (h) release.

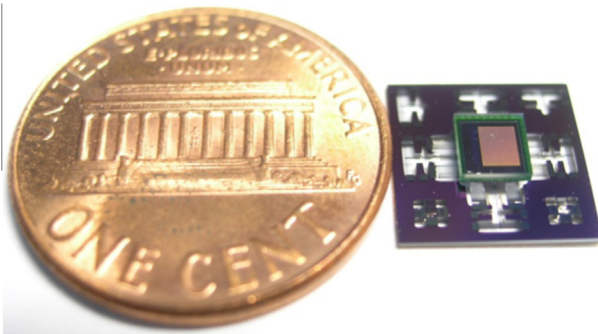

Fig. 10. The *XY* stage after flip–chip bonding.

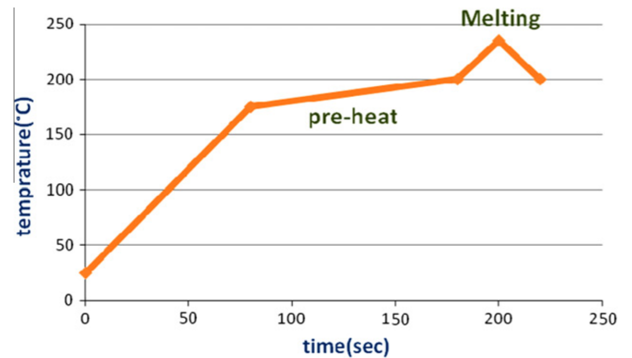

Fig. 12. Reflow profile of flip–chip process.

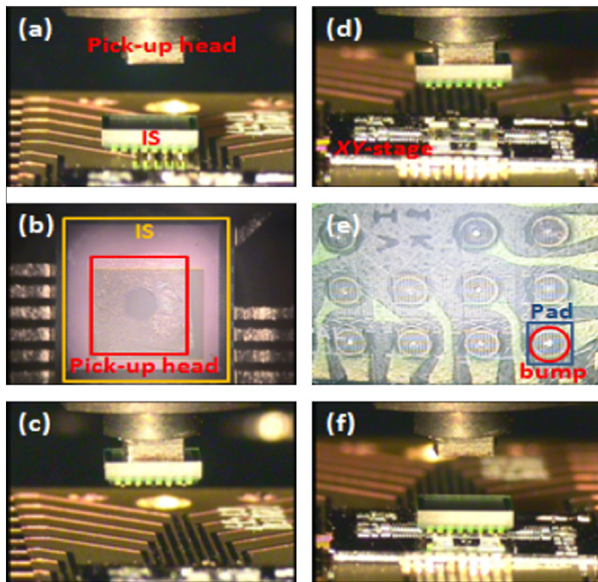

Fig. 11. Flip–chip bonding process of the image stabilizer.

c. Deposit a 1 μm-thick Al layer by DC sputter and pattern as the circuits and pads (Fig. 9c).
d. Pattern the device structure using the first ICP process to a depth of 50 μm (Fig. 9d).
e. Coat and pattern SU8 to isolate heat and electricity in the actuators from the shuttle (Fig. 9e).
f. Use RIE process to pattern the backside oxide layer to be hard mask (Fig. 9f).
g. Use the second ICP process to open the suspending area on the back of the SOI wafer (Fig. 9g).
h. Release the structure by RIE process (Fig. 9h).

4.2. Flip–chip bonding

Fig. 10 shows an IS combined with the proposed image stabilizer by flip–chip approach. Fig. 11 depicts the packaging process captured on the flip–chip bonder monitor. Fig. 11a–c shows the

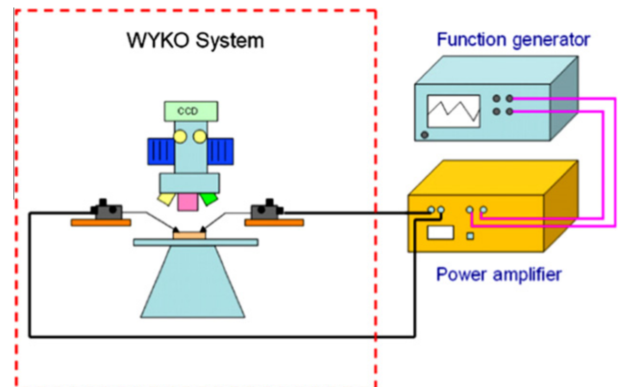

Fig. 13. MMA system.

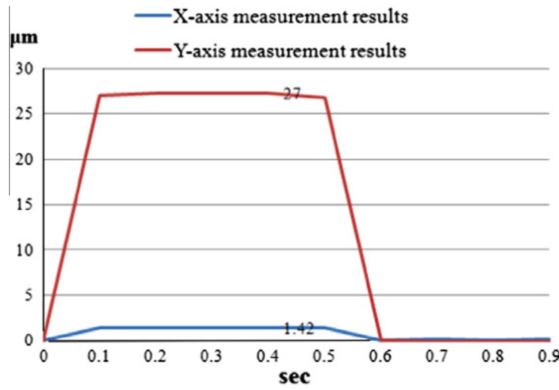

Fig. 14. Displacement of *x*- and *y*-direction on 14 V.

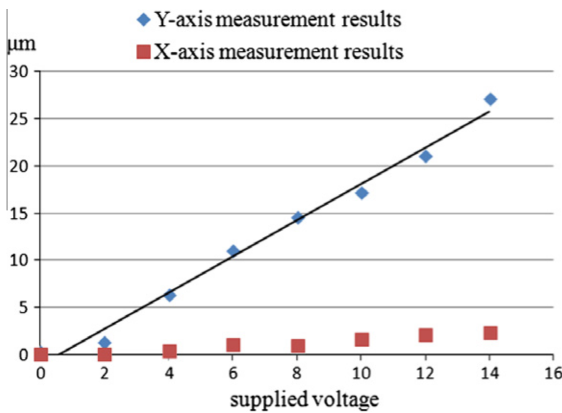

Fig. 15. Static measurement of *XY* stage in *x*- and *y*-directions.

IS absorbing process. Before absorption, the spectroscope is used to align the pick-up head and sensor (Fig. 11b). Fig. 11d–f shows how the sensor bumps and pads of *XY* stage are aligned by the combined processes of the *XY* stage and IS. Fig. 11e and f shows how 3 N force is applied to the IS before the bumps are reflowed to 235 °C, and Fig. 12 shows the reflow profile.

5. Results and discussion

Experiments performed to test the effectiveness of the proposed image stabilizer included a static driving test with the actuator driven by a DC voltage and actuator displacement measured with a MEMS motion analyzer (MMA) (Fig. 13). When a 14-V square wave was applied to the proposed device in the *y*-direction, moving displacement in the *y*-direction was 27 μm, and displacement in the *x*-direction was only 1.42 μm (Fig. 14). The experimental decoupling ratio in the two directions was 19, which conforms to the minimum ratio of 10 required by the system. Fig. 15 shows how displacement varies with driving voltage. The MMA system was also used in the dynamic characterization to evaluate the resonant frequency of the proposed image stabilizer. Fig. 16 shows that although system resonant frequency approximates 4485 Hz, the operating bandwidth is determined by the thermal time constant. In this case, Fig. 17 shows the step wave test results for the thermal actuating *XY* stage, and the device has a rising time of 21 ms.

Fig. 18 shows the measurement results for thermal imaging. The red[1] and blue triangles represent the maximum and the minimum temperatures of the actuator, respectively, when 10 V is applied at 1 Hz. The figure shows that the maximum temperature

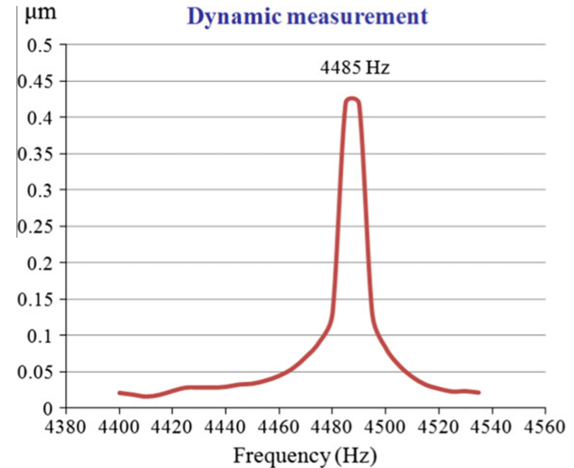

Fig. 16. Measurement results for resonant frequency without IS.

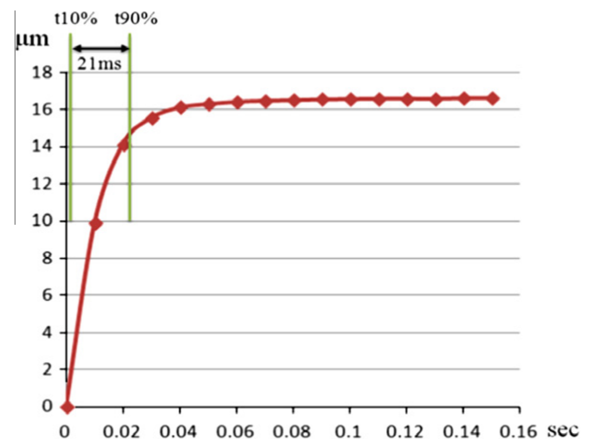

Fig. 17. Step wave test in 10 V.

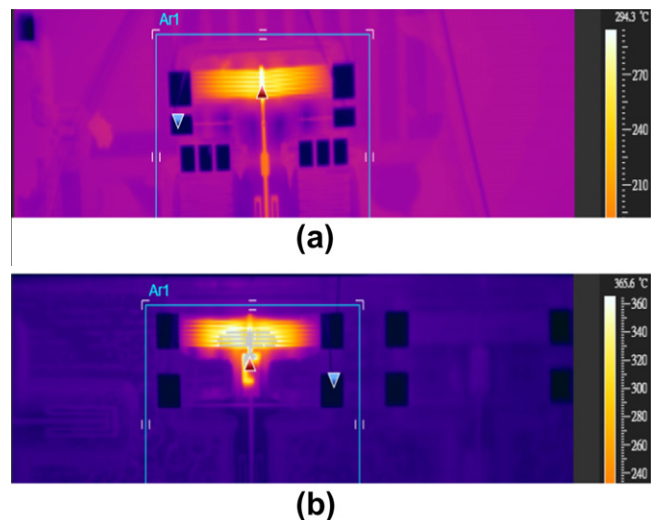

Fig. 18. Measurement results for thermal imaging in 10 volts 1 Hz. (a) Thermal actuator without isolator. (b) Thermal actuator with isolator.

occurs in the middle of the actuator and that the pads approach room temperature. Additionally, comparison of Fig. 18a and b shows that the maximum temperature of the thermal actuator is about

[1] For interpretation of color in Figs. 1–18, the reader is referred to the web version of this article.

290 °C when it is not connected to the isolator and about 360 °C when it is connected to the isolator. Therefore the isolator design enables a lower driving voltage to achieve the same actuating displacement.

6. Conclusion

This work simulated, fabricated, and tested a novel design for an integrated micro decoupling *XY* stage. The integrated *XY* stage is designed to load an IS. The IS was accurately bonded to the shuttle by flip–chip bonding method. The electrical signals of the IS were also connected to the output circuits according to the signal spring design. The proposed *XY* stage has potential applications in commercially available cell phone cameras owing to its anti-shaking function. The main components of the proposed device are a silicon-based *XY* stage and chevron thermal actuators fabricated and packaged with two ICP etching processes by flip–chip bonding technique. Experimental results indicate that a driving voltage of 14 V produces a 27 μm displacement in the driving direction and a 1.42 μm displacement in the vertical direction, which are sufficient for effective anti-shaking. The results for the perpendicular direction are similar since the design is symmetrical. Some variation between the simulation and the experimental results from the undercutting of thermal actuators during ICP etching as well as room temperature variations. The natural frequency of the proposed *XY* stage design approximates 4485 Hz, and the response time approximates 21 ms when measured by MMA system. The isolator SU8 not only insulates the heat flux and driving current, it also increases actuating displacement given a similar driving voltage.

Acknowledgments

This work was supported in part by National Science Council, Taiwan, under Contract 100-2220-E-009-032, 100-2220-E-009-019, and in part by Taiwan Department of Health Clinical Trial and Research Center of Excellence under Contract Nos. DOH99-TD-B-111-004 and DOH99-TD-C-111-005. This work was also supported in part by the UST-UCSD International Center of Excellence in Advanced Bio-engineering sponsored by the Taiwan National Science Council I-RiCE Program under Grant No. NSC-100-2911-I-009-101. This paper is particularly supported by "Aim for the Top University Plan" of the National Chiao Tung University and Ministry of Education, Taiwan, ROC.

References

[1] Sun Lining, Wang Jiachou, Rong Weibin, Li Xinxin, Bao Haifei. A silicon integrated micro nano-positioning *XY*-stage for nano-manipulation. J Micromech Microeng 2008;1(8):125004.
[2] Takahashi Kazuhiro, Mita Makoto, Toshiyoshi Hiroyuki Fujitaand Hiroshi. A high fill-factor comb-driven *XY*-stage with topological layer switch architecture. IEICE Electron Express 2006;3:197–202.
[3] Kwon HN, Lee J-H, Takahashi K, Toshiyoshi H. Micro *XY* stages with spider-leg actuators for two-dimensional optical scanning. Sens Actuator A Phys 2006;130–131:468–77.
[4] Kwon S, Lee LP. Stacked two dimensional micro-lens scanner for micro confocal imaging array. In: Proceedings IEEE MEMS '02; 2002. pp. 483–6.
[5] Laszczyk K, Bargiel S, Gorecki C, Krezel J. Towards integration of glass microlens with silicon comb-drive *X–Y* microstage. In: IEEE/LEOS international conference on optical MEMS and nanophotonics; 2008. pp. 168–9.
[6] Yasumura KY, Grade JD, Jerman H. Fluid damping of an electrostatic actuator for optical switching applications. In: Proceedings solid-state sensor, actuator and microsystems workshop; 2002. pp. 358–61.
[7] Takahashi K, Kwon HN, Mita M, Saruta K, Lee J-H, Fujita H, et al. A silicon micromachined f–θ microlens scanner array by double-deck device design technique. IEEE J Sel Top Quantum Electron 2007;13:277–82.
[8] Yang JP, Mou JQ, Chong NB, Lu Y, Zhu H, Jiang Q, et al. Probe recording technology using novel MEMS devices. Microsyst. Technol 2007;13:733–40.
[9] Ando Y. Development of three-dimensional electrostatic stages for scanning probe microscope. Sens Actuator A 2004;114:285–91.
[10] Indermuhle PF, Linder C, Brugger J, Jaecklin VP, de Rooij NF. Design and fabrication of an overhanging *XY*-microactuator with integrated tip for scanning surface profiling. Sens Actuator 1994;43:285–91.
[11] Kawai Y, Ono T, Esashi M, Meyer E, Gerber C. Resonator combined with a piezoelectric actuator for chemical analysis by force microscopy. Rev Sci Instrum 2007;7(8):063709.
[12] Vancura C, Ruegg M, Li Y, Lange D, Hagleitner C, Brand O, Hierlemann A, Baltes H. Magnetically actuated CMOS resonant cantilever gas sensor for volatile organic compounds. In: Proceedings 12th international conference on solid state sensors, actuators and microsystems; 2003. pp. 1355–8.
[13] Sasaki M, Bono F, Hane K. *XY*-stage for scanning media for optical data storage. In: Proceedings IEEE optical MEMS and their applications; 2006. pp. 36–7.
[14] Kim CH, Jeong HM, Jeon JU, Kim YK. Silicon micro *XY*-stage with a large area shuttle and no-etching holes for SPM-based data storage. J Microelelctrmech Syst 2003;12:470–8.
[15] Lu MS-C, Fedder GK. Position control of parallel-plate microactuators for probe-based data storage. J Microelectromech Syst 2004;13:759–69.
[16] Liu X, Kim K, Sun Y. A MEMS stage for 3-axis nanopositioning. J Micromech Microeng 2007;17:1796–802.
[17] Mukhopadhyay D, Dong J, Pengwang E, Ferreira PM. A SOI MEMS based 3-DOF planar parallel-kinematics nanopositioning stage. Sens Actuator A 2008;147:340–51.
[18] Gu Lei, Li Xinxin, Bao Haifei, Liu Bin, Wang Yuelin, Liu Min, et al. Single-wafer-processed nano-positioning *XY*-stages with trench-sidewall micromachining technology. J Micromech Microeng 2006;16:1349–57.
[19] Yeom DH, Park NJ, Jung SY. Digital controller of novel voice coil motor actuator for optical image stabilizer. In: International conference on control, automation and systems; 2007. pp. 2201.
[20] Sato K, Ishizuka S, Nikami A, Sato M. Control techniques for optical image stabilizing system. IEEE Trans Consum Electron 2005;39:461–6.
[21] Okamoto Yasuhiro, Yoshida Ryuichi. Development of linear actuators using piezoelectric elements. Electron Commun Jpn Part III 1998;81:11–7.
[22] Chen Guan-Rong, Yeh Yeou-Min, Wang Sheng-Jyh, Chiang Huang-Cheng. A novel structure for digital image stabilizer. In: IEEE Asia–Pacific conference on circuits and systems; 2000. pp. 101–4.
[23] Mohamed A, Elsimar H, Ismail M. Analysis, and optimization of a CMOS vertical thermal actuator. In: Proceedings symposium design, test, integration and packaging of MEMS/MOEMS; 2003. pp. 214–7.
[24] Sachs D, Nasiri S, Goehl D. Image stabilization technology overview. <http://www.invensense.com/shared/pdf/ImageStabilizationWhitepaper_051606.pdf>.
[25] Lee Chih-Chun, Chen Wen-Chih, Lee Sz-Yuan, Fang Weileun. Design and implementation of a novel polymer joint for thermal actuator current and thermal isolation. IEEE MEMS Conf 2010:156–9.
[26] Que L, Park J-S, Gianchandani YB. Bent-beam electro-thermal actuators for high force applications. J Micro Electro Mech Syst 1999:31–6.
[27] Lin Chun-Ying, Chiou Jin-Chern. Design, fabrication and actuation of 4-axis thermal actuating image stabilizer. Micro Nano Lett 2011;6(7):549–52.